



ELSEVIER

Available online at [www.sciencedirect.com](http://www.sciencedirect.com)

ScienceDirect

[www.elsevier.com/locate/jmbbm](http://www.elsevier.com/locate/jmbbm)



## Short Communication

# In vivo measurement of skin surface strain and sub-surface layer deformation induced by natural tissue stretching



Raman Maiti<sup>a,\*<sup>1</sup></sup>, Lutz-Christian Gerhardt<sup>b,\*<sup>1</sup></sup>, Zing S. Lee<sup>a</sup>, Robert A. Byers<sup>c</sup>, Daniel Woods<sup>d</sup>, José A. Sanz-Herrera<sup>e</sup>, Steve E. Franklin<sup>a,b,c</sup>, Roger Lewis<sup>a</sup>, Stephen J. Matcher<sup>c</sup>, Matthew J. Carré<sup>a</sup>

<sup>a</sup>Department of Mechanical Engineering, University of Sheffield, UK

<sup>b</sup>Philips Research, Department of Smart Interfaces and Modules, Eindhoven, The Netherlands

<sup>c</sup>Department of Materials Science and Engineering, University of Sheffield, UK

<sup>d</sup>Michelson Diagnostics Limited, Maidstone, Kent, UK

<sup>e</sup>Abengoa Research, Seville, Spain

## ARTICLE INFO

### Article history:

Received 2 March 2016

Received in revised form

24 May 2016

Accepted 30 May 2016

Available online 5 June 2016

## ABSTRACT

Stratum corneum and epidermal layers change in terms of thickness and roughness with gender, age and anatomical site. Knowledge of the mechanical and tribological properties of skin associated with these structural changes are needed to aid in the design of exoskeletons, prostheses, orthotics, body mounted sensors used for kinematics measurements and in optimum use of wearable on-body devices. In this case study, optical coherence tomography (OCT) and digital image correlation (DIC) were combined to determine skin surface strain and sub-surface deformation behaviour of the volar forearm due to natural tissue stretching. The thickness of the epidermis together with geometry changes of the dermal-epidermal junction boundary were calculated during change in the arm angle, from flexion (90°) to full extension (180°). This posture change caused an increase in skin surface Lagrange strain, typically by 25% which induced considerable morphological changes in the upper skin layers evidenced by reduction of epidermal layer thickness (20%), flattening of the dermal-epidermal junction undulation (45–50% reduction of flatness being expressed as Ra and Rz roughness profile height change) and reduction of skin surface roughness Ra and Rz (40–50%). The newly developed method, DIC combined with OCT imaging, is a powerful, fast and non-invasive methodology to study structural skin changes in real time and the tissue response provoked by mechanical loading or stretching.

© 2016 The Authors. Published by Elsevier Ltd. This is an open access article under the CC BY license (<http://creativecommons.org/licenses/by/4.0/>).

\*Corresponding authors.

E-mail addresses: [R.maiti@sheffield.ac.uk](mailto:R.maiti@sheffield.ac.uk) (R. Maiti), [Lutz.Gerhardt@philips.com](mailto:Lutz.Gerhardt@philips.com) (L.-C. Gerhardt).

<sup>1</sup>Both authors contributed equally to this work.

## 1. Introduction

Skin is a complex living organ with non-linear viscoelastic material properties and composed of three main layers: the epidermis, dermis and hypodermis (Gerhardt et al., 2012; Lamers et al., 2013; Weickenmeier et al., 2014). The epidermis, the top layer of the skin, consists of stratum corneum (SC), stratum lucidum, stratum granulosum, stratum spinosum and stratum basale. The stratum corneum acts as a barrier for pathogens entering the skin and prevents unregulated loss of water (Proksch et al., 2008).

It is important to know more about the mechanical, physiological and morphological structural response of skin tissue during contact with equipment or product surfaces, when skin is subjected to static or cyclic shear loading as for example experienced in various sports, consumer lifestyle or medical applications. Previous studies have applied different techniques and methods to better understand skin mechanical behaviour and deformation properties, such as biaxial tensile testing (Huang et al., 2014), sonography (Diridollou et al., 1998; Aoi et al., 2009; Barbarino et al., 2011), histology (Greaves et al., 2014), laser skin microscopy (Lademann et al., 2007), dynamic mechanical analysis/rheometry (Gerhardt et al., 2012; Lamers et al., 2013), video/optical camera setups (Jacquemoud et al., 2007; Kwiatsowska et al., 2009; Mahmud et al., 2010; Ottenio et al., 2015), indentation tests (Pailler-Mattei et al., 2008; Zahouani et al., 2009; Genovese et al., 2015; Kao et al., 2016), magnetic resonance (Barbarino et al., 2011), ultrasound imaging (Weickenmeier et al., 2014), optical coherence tomography (Barton et al., 2003; Neerken et al., 2004; Gambichler et al., 2006; Enfield et al., 2011; Josse et al., 2011; Liu et al., 2013; Tsugita et al., 2013; Zafar et al., 2014; Zhang et al., 2014; Gambichler et al., 2015; Trojahn et al., 2015) and digital image correlation (DIC) (Evans and Holt, 2009; Kwiatsowska et al., 2009; Gerhardt et al., 2012; Ní Annaidh

et al., 2012; Lamers et al., 2013; Buganza Tepole et al., 2014; Affagard et al., 2015; Obropta and Newman, 2015).

Optical coherence topography (OCT) has been used to study vascular morphology using correlation mapping (Enfield et al., 2011; Zafar et al., 2014; Zhang et al., 2014; Byers et al., 2016) and measuring epidermal thickness of various body skin sites (Barton et al., 2003; Neerken et al., 2004; Gambichler et al., 2006; Josse et al., 2011; Tsugita et al., 2013; Trojahn et al., 2015). In addition to the epidermal thickness, Egawa et al. (2002), Li et al. (2006), and Trojahn et al. (2015) measured the arithmetic mean roughness, Ra, and mean depth roughness, Rz, of the top skin surface (stratum corneum).

The details from various imaging studies on the volar forearm that are most relevant for the current work are listed in Tables 1 and 2.

Most of the forearm studies using OCT have never considered angular variations of the volar forearm relative to the biceps/upper arm, variations of the angle of the elbow joint. Though DIC has been performed in both in-vitro and in-vivo conditions (Ní Annaidh et al., 2012; Buganza Tepole et al., 2014; Affagard et al., 2015; Obropta and Newman, 2015), to our knowledge only one study (Obropta and Newman, 2015) considered the effect of changing arm angle on skin surface strain fields of the elbow joint; the arm angle being defined as the angle between the upper arm and lower forearm at the elbow joint. On changing the arm angle from 180° full extension to 90° flexion, the percentage change of the principal strains of the elbow joint (crease of elbow) varied between –41% in anterior (compressive strain) and 44% in posterior sides (tensile strain) (Obropta and Newman, 2015).

To the authors' knowledge, none of the published OCT studies have reported the measurement of epidermal thickness during the change in arm angle in the volar forearm. It is deemed, however, that it is necessary to link the natural skin stretching induced by change in arm angle, to a change in epidermal thickness and surface strain.

**Table 1 – Epidermal thickness of volar forearm skin reported in the literature.**

Author	System information	Sample size and age	Thickness – mean $\pm$ SD ( $\mu\text{m}$ )
Neerken et al. (2004)	Fibre-based optical interferometer (Philips Research)	Young age group: 7 Caucasian females, 8 males (19–24 years) Older age group: 5 females, 10 males (54–57 years)	Young: $89 \pm 9$ Aged: $75 \pm 7$
Weissman et al. (2004)	SkinDex 300 (ISIS Optronics)	n.a	$88.2 \pm 11.9$ (Range: 60–110)
Gambichler et al. (2006)	SkinDex 300 OCT imaging system (ISIS Optronics)	71 samples from Caucasian (41 males and 30 females) groups of young (20–40 years) and aged volunteers (60–80 years)	Young: $71.8 \pm 10$ , Aged: $60.8 \pm 7.4$
Josse et al. (2011)	SkinDex 300 OCT imaging system (ISIS Optronics)	5 female aged 20–35 years (skin type unknown)	$102.4 \pm 7.4$
Abignano et al. (2013)	Vivosight topical OCT probe (Michelson Diagnostics)	22 healthy persons (gender distribution and age unknown)	Range: 80–128
Tsugita et al. (2013)	SkinDex 300 OCT imaging system (ISIS Optronics)	116 sites among 10 Asian (5 female 5 males) volunteers aged between 18–60 years	$66.4 \pm 7.4$
Trojahn et al. (2015)	OCT system Telesto (Thorlabs)	8 samples each from Caucasian female groups of young (31–37 years) and aged volunteers (74–79 years)	Young: $65.1 \pm 8.9$ , Aged: $67.9 \pm 10.5$

**Table 2 – Volar forearm skin surface roughness values reported in literature.**

Author	System information	Age and sample size	Roughness - mean $\pm$ SD ( $\mu\text{m}$ )
Egawa et al. (2002)	Confocal scanning microscope HD100D (Lasertec Corporation)	12 healthy volunteers aged between 21–45 years	Ra: $20.5 \pm 4$ , Rz: $71 \pm 10.1$
Jacobi et al. (2004)	PRIMOS optical 3D skin measurement device (GF Messtechnik)	23 healthy volunteers aged 23–65 years	Ra: $30.0 \pm 5.0$ , Rz: $200.0 \pm 25.0$
Kampf and Ennen (2006)	3D skin analyser (Hommelwerke GmbH)	25 subjects	Ra: $100.2 \pm 19.7$
Li et al. (2006)	Interference fringe Projection (Optics Laboratory)	50 healthy Caucasian Women aged 20–74 years	Ra: $21.8 \pm 7.1$
Bloemen et al. (2011)	PRIMOS optical 3D skin measurement device (GF Messtechnik)	60 subjects aged above 12 years	Ra: $19.6 \pm 5.4$ , Rz: $267.0 \pm 90.3$
Luther et al. (2012)	PRIMOS 4.0 skin measurement device (GF Messtechnik)	18 healthy male (6 from each Caucasian, Asians and Africans) aged 23–32 years	Ra for Caucasian: $26.8 \pm 4.9$ , Ra for African: $22.5 \pm 5.9$ , Ra for Asians: $26.0 \pm 2.6$
Kottner et al. (2013)	PRIMOS 5.7 skin measurement device (GF Messtechnik)	12 healthy young subjects with mean age $32.9 \pm 7.2$ years	Ra: $7.2 \pm 1.3$ , Rz: $35.7 \pm 6.6$
Trojahn et al. (2015)	OCT system Telesto (Thorlabs)	8 samples each, Caucasian female groups of young (31–37 years) and aged volunteers (74–79 years)	Ra for Young: $38.2 \pm 4.3$ , Ra for Aged: $46.5 \pm 7.1$

During body movement the skin is stretched as skin layers are firmly connected with each other and via fascia, muscle and tendons attached to the skeleton. Therefore it is plausible to expect that skin stretching induced by changes of the arm angle will cause changes in skin morphology and surface topography.

High and low strain regions observed on the skin can be used for example in the design of tissue engineered skin implants for plastic surgery and design of exoskeletons, prostheses, orthotics, or comfort optimised wearable devices to determine the accurate placement on the body site. This information could also aid in the design of sensors to reduce noise artefacts and improve user comfort for kinematics measurements (Obropta and Newman, 2015).

The aim of this case study was to investigate the feasibility of using OCT to reliably quantify morphological changes in the upper skin layers and sub-surface (stratum corneum, epidermis, and dermal-epidermal junction) due to natural forearm skin stretching and to correlate the results with surface strains measured by DIC. To the best of the authors' knowledge, this is the first study to combine the two non-invasive methods, namely DIC and OCT, to measure strains on the skin surface and deformation of sub-surface layers based on geometrical changes of deeper tissue layers respectively. The objectives of the study were to (1) measure surface strain using DIC induced by changing the arm angle, (2) determine epidermal thickness and through-plane skin layer deformation (e.g. flattening of dermal-epidermal junction)

and change in skin surface roughness from analysing OCT images.

## 2. Materials and methods

### 2.1. Test subjects

The right arm of a 38-year old Caucasian male was used in this case study with forearm shaven the evening before the experiment to avoid interference of hair follicles in the experiments. The skin was cleaned with an alcohol wipe before any experiments were conducted. The study protocol was approved by the University of Sheffield (Ethics Number 002074). The volunteer signed informed consent before any tests were started.

### 2.2. Digital image correlation (DIC)

DIC is an optical-numerical full field measuring technique, which offers the possibility of determining complex displacement and deformation fields at the surface of objects under any kind of loading. DIC has been traditionally used to study deformation of engineering materials (Sutton et al., 2009) but has attracted increasing interest in the biomedical and experimental biomechanics field because it allows the characterisation of biological tissues, organs and their interactions with biomedical devices (Palanca et al., 2016; Hu et al., 2016).

The principle of DIC relies on tracking random patterns (Fig. 1) on a material surface subjected to deformation. A suitable software recognises and locates the corresponding patterns covered through the surface before and after deformation, using an image correlation algorithm. The pattern is recorded using a digital camera before and after deformation. The whole displacement field on the specimen surface is then determined by correlating two subsequent images.

In DIC, a random pattern is applied to the surface of an object with sufficient contrast that can be tracked from image to image by comparing images in the deformed configuration with a reference configuration (Fig. 1). To process and enable the correlation, the images are divided into small subsets of a number of pixels. Within the subset, there must be a well captured and recognisable greyscale distribution.

Images of the deformed states are compared to the reference in order to match subsets and track the displacement (Fig. 1). The degree of matching between subsets is evaluated by a cross-correlation function (Sutton et al., 2009; Palanca et al., 2016). For more details, the reader is referred to publications from Sutton et al. (2009) and Palanca et al. (2016).

In the current study, the random pattern applied on the volar forearm skin is shown in Figs. 1 and 2a. A black water-based ink (Crafters Acrylic Paint, DecoArt Inc., Stamford) was used on the forearm and was distributed randomly by flicking the bristles of a toothbrush. For acquisition of images, two Pike F505B cameras (Allied Vision Technologies GmbH, Germany) equipped with monochromatic CCD sensor (Sony ICX625; 2/3"; 2452 × 2054 pixels) and 50 mm lens objectives (XENOPLAN 2.8/50-0902, Schneider, Kreuznach) were placed along the sagittal plane (plane dividing the human body into left and right halves) as shown in Fig. 2b. The two cameras were used to be able to accurately determine in-plane deformations of curved 3D surfaces (i.e., the uneven skin surface) and minimise errors of the measured in-plane skin displacement fields (Sutton, 2008).

The stereo angle between the two cameras was 30°. The distance of the cameras to the volar forearm was about 350 mm, which resulted in field of view of 47 × 39 mm<sup>2</sup>. Measurements were carried out at 20–22 °C, 40–50% relative

humidity. Following to the setup and the resulting field of view, the spatial pixel resolution was about 0.02 mm/pixel. Due to the comparable large diameter of the average speckle pattern generated, the subset for the evaluation (Fig. 1) has to be chosen comparable large (81 × 81 pixels) compared to the minimum speckle size of 3 × 3 pixels such as recommended in the testing guide of the used digital image correlation software VIC-3D of Correlated Solutions (VIC-3D v7 Testing Guide, 2016). However due to the smooth curvature of the object surface compared to the speckle size as well as the relatively homogeneous strain distribution further optimisation was not required for these tests.

Prior to data collection, the camera system was calibrated using VIC-3D Digital Image Correlation software (version 7.2.1, Correlated Solutions, USA) and a known grid size pattern (2 mm grid, 11 × 10 grid points; calibration score: 0.037 pixels). The forearm set-up and the cameras remained fixed through the experiment. Hence, multiple calibrations of the system were not required.

Images were captured at 5 frames per second. An ordinary fluorescent white light source was used to illuminate the skin surface during the experiment. The displacements and strain have been evaluated by the software VIC-3D. The coordinates were set in a way that the X-axis was pointing from lateral to medial side of the forearm and the Y-axis pointing from wrist to elbow-joint (Figs. 1a and 2a). To determine the noise level (e.g. noise due to motion artefacts, light instabilities or pulsation of blood flow through the volar forearm) and consequently measurement sensitivity of the skin DIC measurement setup, the first and last three consecutive stationary images of each flexion-extension cycle and image sequence were analysed. The typical noise level and sensitivity of skin displacement measurements was less than 200 µm. The noise level of the Lagrange strain measurement was about 0.03–0.04%. Both noise levels and measurement sensitivities were determined from the mean standard deviations of several sets of two consecutive 'still' images in the 90° bending position.

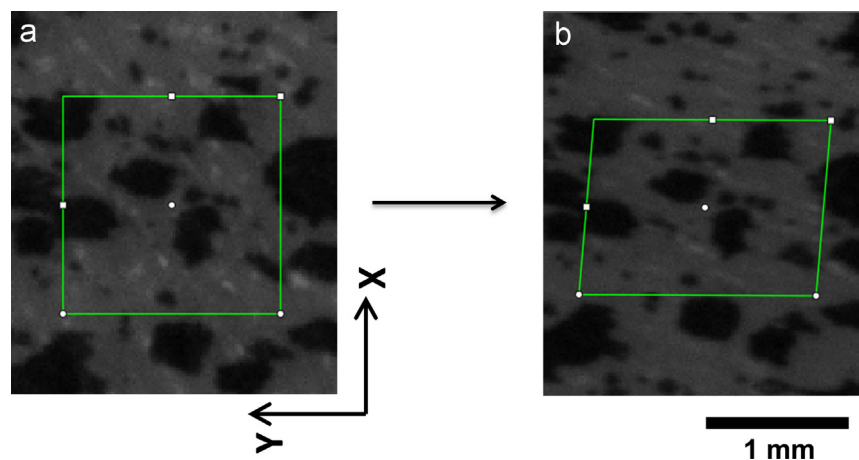


**Fig. 1 – Random spray pattern with subset and central subset pixel point (green boxes) superimposed on images for calculation of skin surface deformation and related strains. a) Un-deformed skin surface (reference configuration) and b) deformed skin surface. For interpretation of the references to color in this figure legend, the reader is referred to the web version of this article.**

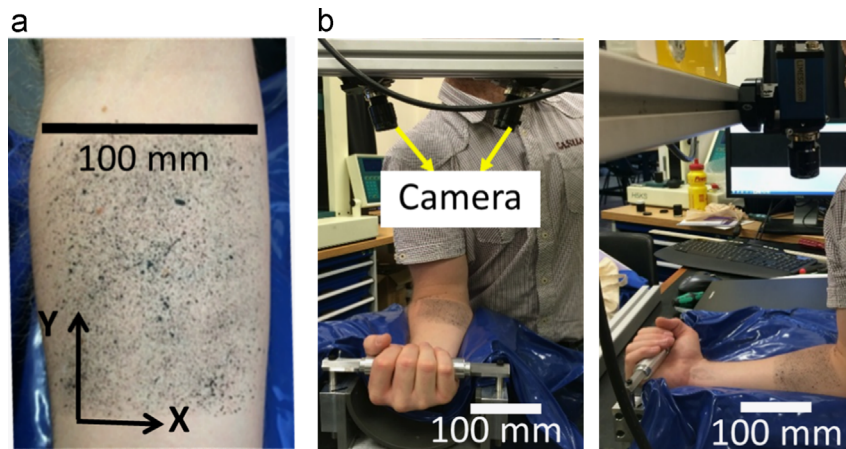


**Fig. 2 – a)** Definition of coordinate system for DIC measurements. Spray pattern on forearm shown along with superimposed X-Y coordinate system defined for surface strain measurements, **b)** DIC set-up showing the positioning of the two cameras.

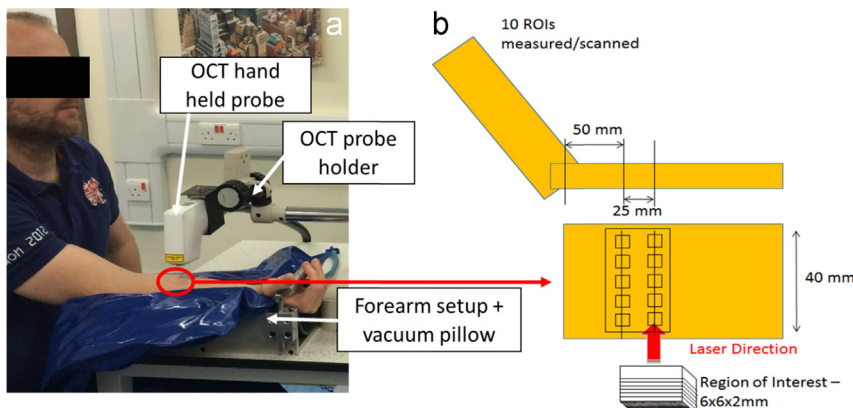


**Fig. 3 – a)** OCT measurement setup, **b)** schematic of volar forearm: regions of interest and scan dimensions.

### 2.3. Optical coherence tomography (OCT)

OCT is a non-invasive technique based on the principle of light interference (Gambichler et al., 2015). A surface is detected based on the interference of two waves, one passing through the surface with the other used as a reference (Fercher et al., 2003). The morphology and structure of volar forearm skin was imaged using clinically approved VivoSight (Michelson Diagnostics, Kent). The VivoSight system is a Fourier domain OCT with a 20 kHz swept source diode laser at 1300 nm centre wavelength, it has 7.5  $\mu\text{m}$  lateral and 5  $\mu\text{m}$  axial resolution with an A-scan (reflectivity) image capture rate of 20 frames per second with each image of  $1342 \times 460$  pixels. For stability, the hand held probe of VivoSight was fixed in the microscope holder (Fig. 3a). Ten regions of interest (ROIs) were measured on the volar forearm 50 mm away from the arm bend.

The 10 regions were located in an area of  $25 \times 40 \text{ mm}^2$  with distance of 5 mm between them as shown in Fig. 3b. The OCT image volume obtained from each ROI was of dimension  $6 \times 6 \times 2$  (width  $\times$  length  $\times$  depth)  $\text{mm}^3$ . Measurements were carried out in a climate controlled room at 20 °C, 45–50% relative humidity.

### 2.4. Experimental protocols

The right arm of the volunteer was placed in the arm holder forearm setup as shown in Figs. 3a and 4. A vacuum pillow was used to minimise motion artefacts during the measurements. Whereas OCT images were taken at two quasi-static arm positions, at 90° flexion and 180° full extension (Fig. 4), in skin surface strain measurements (DIC) the full flexion-extension motion was monitored using the two cameras (Fig. 2).

### 2.5. Data analysis

#### 2.5.1. Strain analysis from DIC

The experimental data was analysed using VIC-3D Digital Image Correlation software (version 7.2.1) from Correlated Solutions, Inc. The VIC-3D algorithm matches the same points, obtained from the two different cameras, by comparing the grey value intensity distribution/image intensity variation in a square pixel subset in the reference (undeformed) and deformed configuration, using correlation algorithms developed by Sutton et al. (2009). The matched set of points are used to construct the shape of the object and track 3D surface displacements. For correlating images, a

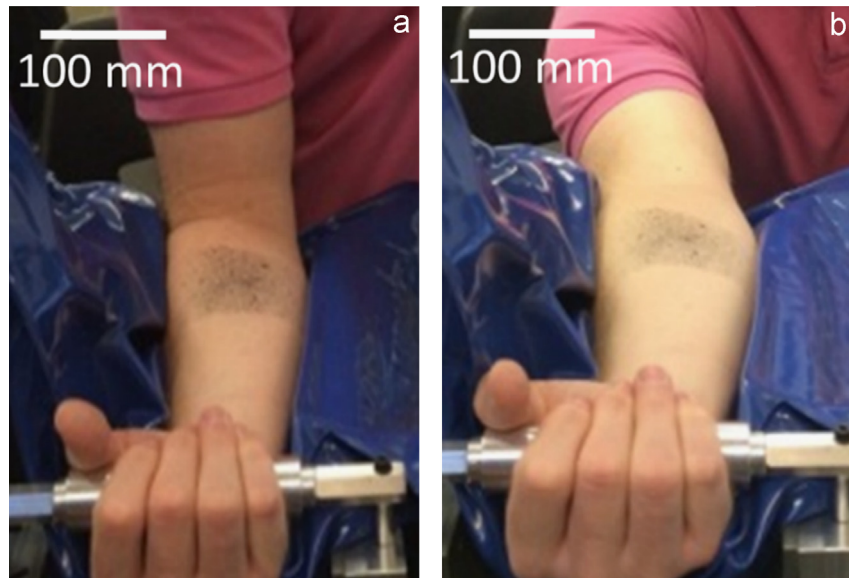


**Fig. 4 – Forearm angles (a) flexion 90° and (b) 180° or full extension. The typical spray patterns can be seen on the volar forearm, from which strain fields were determined.**

subset size of  $81 \times 81$  pixels, step size of 7 pixels and interpolation filter size of 15 pixels were chosen in the current study. The DIC software tracks the movement of the grey-scale distribution within each subset relative to its centre point from image to image to obtain a displacement (Fig. 1). The subset size directly influences the signal-to-noise ratio of the displacements and strains, since the greyscale information within a subset is used for the correlation between images. The step size controls the spacing between the subset centres that are analysed during correlation (Fig. 1).

From the correlated skin displacement field, Lagrange strains (Eqs. (1)–(6)) were calculated because large deformations and strains were expected due to the large angle 90° flexion–180° extension motion induced stretching of the skin; which is considered a fluid-filled soft composite material with non-linear elastic material properties similar to soft elastomers (Gerhardt et al., 2012).

The Lagrange strain tensor  $\mathbf{E}$  was calculated based on a deformation gradient tensor formulation for motion kinematics mapping from a reference to a deformed configuration (Parsons et al., 2004; Sutton et al., 2009), as follows:

$$\mathbf{E}_i = 1/2(\mathbf{F}_i^T \cdot \mathbf{F}_i - \mathbf{I}) = 1/2(\mathbf{C}_i - \mathbf{I}) \quad (1)$$

$\mathbf{E}_i$  being the Green–Lagrange strain tensor of point  $i$  of the random pattern and  $\mathbf{F}_i$  its corresponding deformation gradient based on the reference frame shown in Fig. 2a), namely:

$$\mathbf{F}_i := \frac{\partial \mathbf{x}_i}{\partial \mathbf{X}_i} \quad (2)$$

and  $\mathbf{C}_i$  the right Cauchy–Green deformation tensor and  $\mathbf{I}$  the unit matrix  $[\mathbf{I}] = \begin{bmatrix} 1 & 0 \\ 0 & 1 \end{bmatrix}$ .

The matrix components of tensor  $\mathbf{E}$  are given by

$$: [\mathbf{E}] = \begin{bmatrix} E_{xx} & E_{xy} \\ E_{yx} & E_{yy} \end{bmatrix} \quad (3)$$

Note that tensor components in Eq. (3) are referred to pattern surface and hence evaluated on two orthonormal local axis X, Y, tangent at each point of the pattern. Orientation of these axes is the same than global axes shown in Figs. 1 and 2. Out-of-surface strains are considered to be negligible versus computed membrane (surface) strains, according to the classical hypothesis of thin layer surface kinematics by Timoshenko and Woinowsky-Krieger (1959).

As the matrix  $[\mathbf{E}]$  is symmetrical, by definition  $E_{yx} = E_{xy}$ . By introducing eigenvalues  $\lambda$  in the strain matrix, which by mathematical definition are principal strains when the determinant of the matrix becomes zero, i.e. in associated principal strain directions, the shear components  $E_{xy}$  are null.

$$\begin{vmatrix} E_{xx} - \lambda & E_{xy} \\ E_{xy} & E_{yy} - \lambda \end{vmatrix} = 0 \quad (4)$$

The principal strains  $E_1$  and  $E_2$  were computed from the characteristic polynomial (Eq. (5)):

$$(E_{xx} - \lambda) \cdot (E_{yy} - \lambda) - E_{xy}^2 = 0 \quad (5)$$

Solving the characteristic polynomial of Eq. (5) gives:

$$\lambda_{1,2} = E_{1,2} = \frac{E_{xx} + E_{yy}}{2} \pm \sqrt{\left(\frac{E_{xx} + E_{yy}}{2}\right)^2 + E_{xy}^2} \quad (6)$$

$\lambda_{1,2}$  are eigenvalues of matrix  $\mathbf{E}$  and called principal strains. All the strain measurement data is expressed as relative percentage change at full extension (180°) and reported as means  $\pm 1$  standard deviation (sd). To obtain representative skin strain values, five repeated flexion-extension experiments were carried out at five different locations on the volar forearm. From each experiment, three subsequent stationary images at 90° flexion and 180° extension, respectively, were analysed and compared with each other. Average strain values were determined from more than 3400 data points, defined by and arising from the number of analysed images and chosen subset size.

### 2.5.2. OCT image analyses

B-scan images obtained from OCT measurements were first converted to single tag image file format (tiff) files through ImageJ (ImageJ Developers). Then, the boundaries of the stratum corneum (yellow line in Fig. 5a) and dermal-epidermal junction (DEJ) (green line in Fig. 5a) were determined in each image using a Matlab algorithm (Matlab version R2015a) based on analysis of light reflectivity/backscatter profiles (A-scans).

The Matlab algorithm uses anisotropic filtering to remove speckle noise from the images, using prior knowledge of the multiple channel foci in the multi-beam OCT. A first mean filter is used to remove speckle noise from the images. First, a proprietary filter is used to blend the four multi-beam OCT channels which maximises speckle suppression while maintaining resolution and contrast. A second mean filter is then used (chosen for simplicity and speed) which is not uniform in shape, having a greater size in and giving greater weight to pixels in the X- and Y-dimensions (i.e. laterally). This filter has been chosen to preserve resolution in the axial dimension and therefore minimise blurring of the interface between the epidermis and dermis. The image is then processed using two separate algorithms:

The first of these uses an edge filter designed to detect the air-skin (stratum corneum) boundary by targeting the edge-spike combination caused by the sharp change in refractive index. Candidate edges exceeding a threshold (greater than 30

pixels in size) are recursively used to calculate a confidence figure for each measurement based on surface smoothness and edge-fit and this confidence is used to negate the effect of surface artefacts caused by overlaying hairs or surface "flare" or reject measurements if no satisfactory solution can be found. Finally, the point in each image column with the greatest confidence factor is chosen.

The second was designed to detect the contrast change at the DEJ, where the image changes in character from the grainy keratinocytes of the spinosum to the smoother, mottled and brighter papillary dermis (Abignano et al., 2013). At the position of the meeting of these two skin layers, a hypo-reflective region (typically visible as only a line in OCT images of this resolution) is present, due to the relatively high nuclear-cytoplasmic ratio within the basal membrane (Coleman et al., 2013). Detection of candidates for this surface are selected in a similar manner to the algorithm used to detect the skin surface.

No direct validation exists confirming the selection of the correct morphological feature in this step, but widespread consensus of its identity is present in literature, based on histological correlation (Coleman et al., 2013) and, in the case of pathological morphology, modification of the DEJ in a manner predicted by knowledge of the condition (as investigated by Pomerantz et al. (2011), Sattler et al. (2013), Alawi et al. (2015), Ulrich et al. (2015)).

After boundary tracking/segmentation of stratum corneum and DEJ, algorithms were programmed to determine epidermal

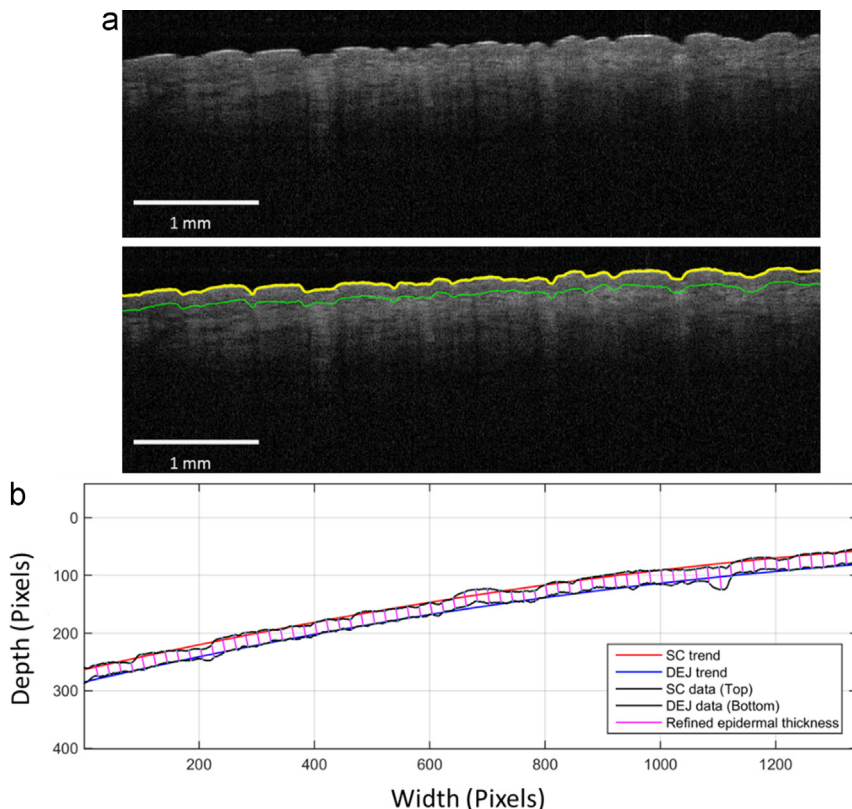


**Fig. 5 – Procedure for determining epidermis thickness.** a) Stratum corneum (SC) and dermal-epidermal junction (DEJ) detection. (b) Thickness determination of epidermis (in pixels) based on skin layer detection. For better readability and representation of the thickness determination procedure, every 22<sup>nd</sup> perpendicular thickness line is plotted. For interpretation of the references to color in this figure, the reader is referred to the web version of this article.

thickness, skin surface roughness and geometrical parameters of the dermal-epidermal junction (flatness). To account for any possible skin curvature in OCT images, the epidermal thickness was calculated by measuring the perpendicular line (approx. 224 lines per mm) between the 3<sup>rd</sup> order polynomial fitted stratum corneum and fitted dermal-epidermal layer junction (Fig. 5b) on the basis of a locally weighted fit and 5-point moving average filter (Matlab command loess with smoothing parameter of 0.1). Epidermal thickness distribution is shown in boxplots and data reported as means thickness  $\pm 1$  sd.

To remove the natural curvature from the surface topography, discriminate between waviness and true surface roughness (topography profile decomposition in waviness and roughness) and be able to reliably determine geometry change of DEJ, the skin line profiles of SC and DEJ layers were trend removed by subtracting 3<sup>rd</sup> order polynomial curve fits of the topographical profile from the full profile (Fig. 6). The 3<sup>rd</sup> order polynomial curve fits was selected based on sensitivity analysis of close match to the trend, and removal of unnecessary undulation in the skin, not required for trend calculation. A third polynomial fit was found to describe best the natural curvature of the OCT images. Higher order fits did not further improve the fitting.

Then, after converting image pixels into distances by dividing pixel numbers by the image resolution (230 pixels/mm), the skin surface roughness and geometry parameters were determined using DIN ISO 1302 standard definitions for arithmetic mean roughness Ra and 10 point roughness depth Rz (see Eqs. (7) and (8)). The average surface roughness Ra is defined as:

$$Ra = \frac{1}{n} \sum_{i=1}^n |y_i| \quad (7)$$

with n being the sample length (total image pixel number) and  $y_i$  the vertical pixel distance from the mean line to the ith data or image pixel point (Fig. 6).

Rz represents the average maximum height of the topographical profile over five equal and consecutive sample length periods, into which the full profile as shown in Fig. 6 was divided per following definition:

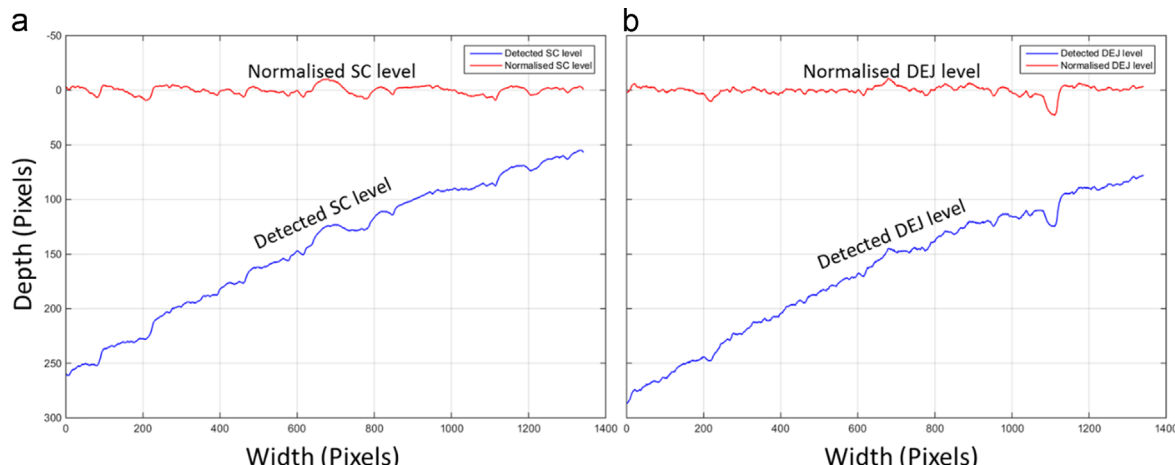


**Fig. 6 – Extracting of roughness (red curves) from topographical skin profiles (blue curves): Roughness of stratum corneum (a) and dermal-epidermal junction (b) (in pixels) was determined by subtraction of 3<sup>rd</sup> order polynomial fits from the profile. For interpretation of the references to color in this figure legend, the reader is referred to the web version of this article.**

$$Rz = \frac{1}{5} \sum_{i=1}^5 Rt_i \quad (8)$$

with:  $Rt_i = \max_i(y_i) - \min_i(y_i)$ , where  $Rt_i$  is the maximum profile height Rt for the ith sampling length. Roughness parameters are presented as means  $\pm 1$  sd.

## 2.6. Statistics

As data was sufficiently well normally distributed and showed sufficiently homogenous variances, paired t-tests were applied to investigate for any significant difference in epidermal layer thickness and skin roughness parameters between 90° flexion and 180° full extension. Probability levels with p values less than 0.05 were considered statistically significant. Statistical analyses were carried out using IBM SPSS Statistics 22 (IBM Hampshire, UK).

## 3. Results

### 3.1. DIC image analysis

The skin surface strain behaviour at 90° arm angle and full extension (180°) is shown in Fig. 7. Fig. 7a shows the initial condition of the arm at 90° flexion. At 180° full extension of the forearm, Lagrange strain ( $E_{yy}$ ) was found to be highest towards the arm bend as shown in Fig. 7b.

The skin towards the elbow joint generally showed higher surface tensile strains  $E_{yy} > 30\%$  as compared to the skin closer to the wrist ( $E_{yy} < 20\%$ ). Average Lagrange strains ( $E_{yy}$ ) were about 23%. The transition of the Lagrange strain from initial condition at 90° flexion to highest strain at 180° full extension can be observed in GIF animated file provided as supplementary material.

The percentage change in compressive, tensile, shear and principal Lagrange ( $E_1, E_2$ ) strains upon skin stretching are tabulated in Table 3. The strain in X and Y direction are, respectively, compressive ( $E_{xx} = -5.6 \pm 1.0\%$ ) and tensile strains ( $E_{yy} = 23.3 \pm 2.2\%$ ) as compared to the 90° arm angle position. DIC showed that natural arm bending from 90° flexion

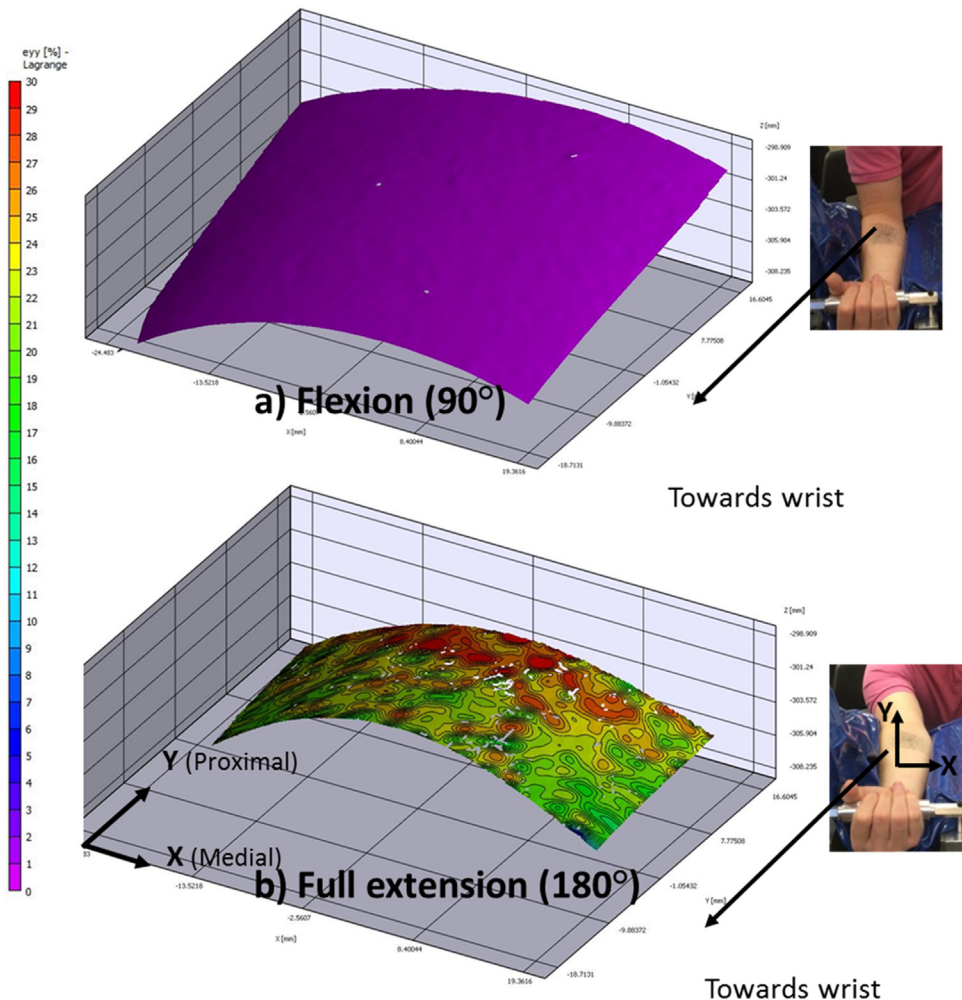


**Fig. 7 – Contour plot: Skin surface strain field ( $E_{yy}$ ) at a)  $90^\circ$  (natural strain) and b) induced strain through full skin extension at  $180^\circ$  arm angle. For definition of coordinate system see Figs. 1 and 2.**

**Table 3 – DIC: Mean skin surface strains at full arm extension at  $180^\circ$ . The values listed are mean values of 5 repeated experiments, in each of which 3 stationary images were analysed from which an average strain or area was calculated.  $E_1$ : tensile principal strain;  $E_2$ : compressive principal strain.**

Strain	$E_{xx}$ [%]	$E_{yy}$ [%]	$E_{xy}$ [%]	$E_1$ [%]	$E_2$ [%]	Area [cm <sup>2</sup> ]
Mean	-5.6	23.3	-7.6	26.1	-8.4	5.9
sd	1.0	2.2	1.7	2.3	1.2	1.1
E <sub>xx</sub> strain along medial forearm direction						
E <sub>yy</sub> strain along proximal forearm direction						

(reference configuration) to full extension is characterised by a multiaxial surface strain distribution/state; however, compressive and shear strains were found to be relatively small (6–8%) compared to  $E_{yy}$  (>20–30%), implying that the tensile component may dominate the overall skin deformation behaviour. As shown in Table 3, repeatability standard deviations were low (<2.3%), indicating a high repeatability of the strain

measurements. Standard deviations within each repeated experiment (i.e., of 3 consecutive stationary images) were considerably lower (<0.2%) compared to repeatability standard deviations.

### 3.2. OCT image analysis

Two examples of images taken during flexion ( $90^\circ$ ) and full extension ( $180^\circ$ ) are shown in Fig. 8. The topography of SC and DEJ layers can be seen in the image of  $90^\circ$  arm angle. Compared to  $90^\circ$  flexion, both the layers smoothed during  $180^\circ$  full extension arm angle.

Following natural stretching and strain induced by changing the arm angle, the epidermal layer thickness reduced significantly ( $p=0.001$ ) by 20% when the arm angle was changed between  $90^\circ$  flexion ( $108\pm14\text{ }\mu\text{m}$ ; median:  $107\text{ }\mu\text{m}$ ) and  $180^\circ$  full extension ( $90\pm12\text{ }\mu\text{m}$ ; median:  $89\text{ }\mu\text{m}$ ) as shown in Fig. 9. Epidermal thickness standard deviations of the means within each ROI (Fig. 3) were comparable with repeatability standard deviations of the ‘pooled’ mean of 600 images.

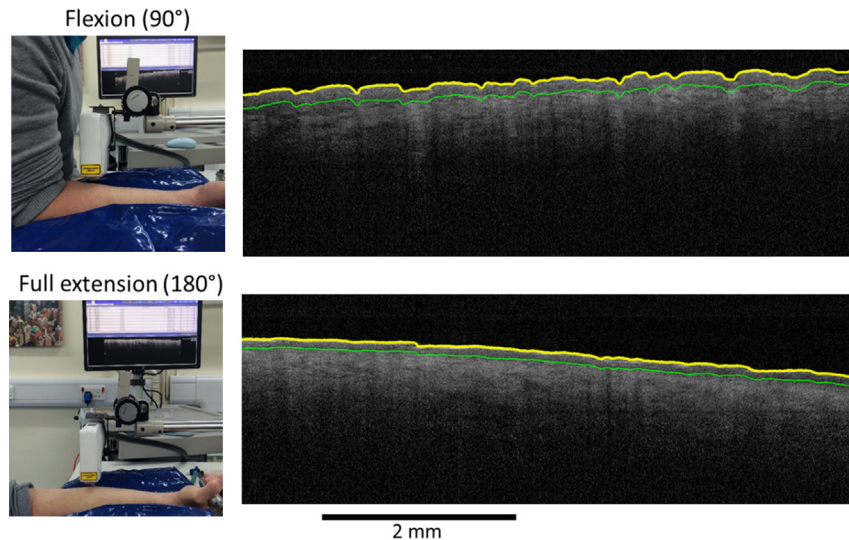


**Fig. 8 – OCT images of stretched and unstretched forearm skin. Qualitatively smoothing of skin surface (stratum corneum) and flattening of dermal-epidermal junction can be observed. Top OCT image: Flexion ( $90^\circ$ ); bottom image: Full Extension ( $180^\circ$ ).**

Skin roughness parameters ( $R_a$  and  $R_z$ ) of the SC and DEJ significantly decreased by up to 45% ( $p=0.001$ ) when the arm angle changed from  $90^\circ$  flexion arm angle to  $180^\circ$  full extension (Table 4). For instance,  $R_a$  changed from  $14.2 \pm 2.6 \mu\text{m}$  and  $15.3 \pm 3.1 \mu\text{m}$  to  $8.4 \pm 2.2 \mu\text{m}$  and  $8.4 \pm 3.5 \mu\text{m}$  for SC and DEJ respectively during  $180^\circ$  full extension arm angle.

#### 4. Discussion

##### 4.1. Skin surface strains and epidermal thickness change

This study aimed to investigate the feasibility of using OCT to reliably quantify, *in vivo*, the topographical and morphological changes in upper skin layers (stratum corneum, epidermis, DEJ) due to natural forearm skin stretching, measured by DIC. While several papers report on the measurements of epidermal thickness based on image analysis of OCT measurements (Neerken et al., 2004; Weissman et al., 2004; Gambichler et al., 2006; Josse et al., 2011; Hojjatoleslami and Avanaki, 2012; Abignano et al., 2013; Tsugita et al., 2013; Trohjan et al., 2015), none of these studies linked skin surface strains to epidermal layer thickness and undulation geometry change of the dermal-epidermal junction.

In the current study, upon natural stretching by changing the volar arm angle from  $90^\circ$  flexion to  $180^\circ$  full extension, the principal tensile strain  $E_1$  of the volar forearm increased by 26% (Fig. 7, Table 3). These volar forearm strain values are lower than skin surface strains measured in the crease of the elbow by Obropta and Newman (2015), with principal strain values ranging from 36–60%. Differences in the anatomical region (crease of elbow), in the average age (23 years old subjects) and body composition of the subjects, or the general test procedure (Obropta and Newman performed an extension-flexion cycle) can be possible explanations for the higher principal skin strains measured by Obropta and Newman (2015).

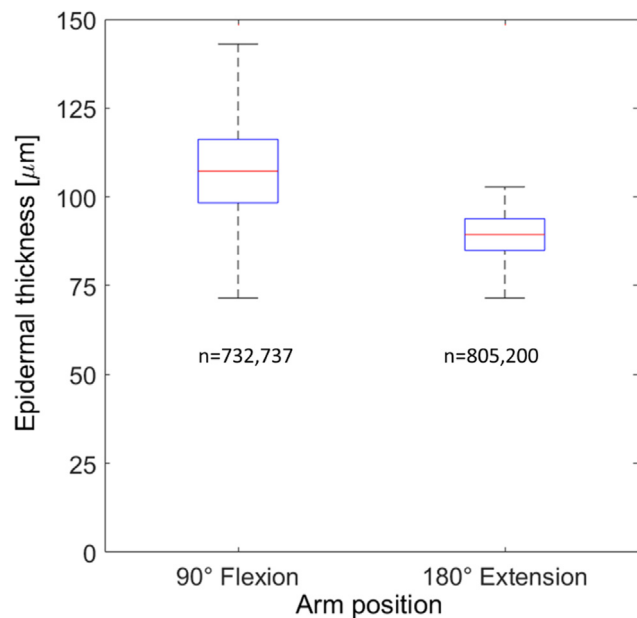


**Fig. 9 – Box plot of epidermal thickness measured before and after stretching at  $90^\circ$  and  $180^\circ$ . The boxplots are made out of thickness value of in total up to 600 images (60 images per ROI, see Fig. 3), each of which contains 1342 individual thickness values.**

In this case study with one test subject, we found that the average epidermal thickness of the volar forearm decreased from 108 to 90  $\mu\text{m}$  when the arm angle was changed from flexion to extension, thereby experiencing an increase in average skin surface strains ( $E_1$ ) of 26%. To our knowledge there is surprisingly no detailed quantitative data available on the effect of *in vivo* or *in vitro* skin stretching on epidermal layer thickness and undulation geometry change of the epidermal-dermal junction. Therefore, more extended research is needed to be able to fully

**Table 4 – Roughness parameters of stratum corneum and dermal-epidermal junction at 90° and 180°. Data is shown as means  $\pm 1$  sd. Each mean is calculated from 600 images (60 images per ROI, see Fig. 3), each of which contains 1342 individual roughness values. Standard deviations within ROIs were comparable with repeatability standard deviations of the mean of ‘pooled’ 600 images.**

Stratum Corneum	Ra [ $\mu\text{m}$ ]	Rz [ $\mu\text{m}$ ]
90° Flexion	14.2 $\pm$ 2.6	75.7 $\pm$ 16.7
180° Full Extension	8.4 $\pm$ 2.2	38.4 $\pm$ 11.0
% Change of mean	–40.7	–49.3
Dermal-epidermal Junction	Ra [ $\mu\text{m}$ ]	Rz [ $\mu\text{m}$ ]
90° Flexion	15.3 $\pm$ 3.1	81.4 $\pm$ 18.6
180° Full Extension	8.4 $\pm$ 3.5	40.4 $\pm$ 15.3
% Change of mean	–45.5	–50.4

validate and generalise our findings. For example, it would be interesting to know the correlation with uniaxial tensile tests on ex vivo human skin, measuring the change in epidermal thickness upon fixing the tissue at a certain strain, or imaging the epidermis in real time during tensile testing.

In general, the observed OCT image derived epidermal thickness values (90–108  $\mu\text{m}$ ) from this case study were fairly in agreement with published data ranging from 60–128  $\mu\text{m}$  (Table 1). Different experimental procedures (e.g. arm angle), study populations and definitions of epidermal thickness, as well as different image processing algorithms (Neerken et al., 2004; Weissman et al., 2004; Gambichler et al., 2006; Josse et al., 2011; Hojjatoleslami and Avanaki, 2012; Abignano et al., 2013; Tsugita et al., 2013; Trojahn et al., 2015) can have influence on the measured thickness and partially explain the relatively large range of epidermal thickness determined from OCT images (Table 1).

In our study, we determined the thickness of the epidermis using speckle noise reduced images, boundary tracking of stratum corneum and DEJ, locally weighted moving average filtering of boundary traced curves, and orthogonal vector matching between both fitted curves. Neerken et al. (2004) measured the epidermal thickness based on analysis of OCT image intensity profiles, and in this case the determination of the epidermal thickness was strongly dependent on the definition of reference markers (e.g. on top or in the valleys of dermal papillae as arbitrarily chosen by the authors (Neerken et al., 2004). Therefore, due to the undulation of the DEJ, large differences can be obtained in epidermis layer thickness. For example, Weissman et al. (2004) used a novel shapelet-based image processing technique for the automatic identification of the upper and lower boundaries of the epidermis in living human skin tissue. These boundaries were used to determine epidermal thickness, with values ranging between 60 and 110  $\mu\text{m}$  (Weissman et al., 2004). Although being beyond the scope of this paper, it would be interesting to compare the robustness and performance of our algorithm with the various image algorithms reported in the literature and compare all the results which histological analyses.

#### 4.2. Skin topography and DEJ geometry and undulation change

In this case study, upon changing the forearm angle from 90° bending to 180° extension, the mean skin surface roughness Ra decreased from 14.2  $\mu\text{m}$  to 8.4  $\mu\text{m}$  (Table 4). In both arm positions the roughness Ra was found to be lower than average values (20.5–100.2  $\mu\text{m}$ , see Table 2) measured by Egawa et al. (2002), Jacobi et al. (2004), Kampf and Ennen (2006), Li et al. (2006), Bloemen et al. (2011), Luther et al. (2012) and Trojahn et al. (2015). Different experimental techniques (e.g. laser scanning microscopy of silicone rubber based skin replicas in Egawa et al. (2002) and Li et al. (2006), study populations, test protocols and roughness profile algorithms (e.g. different filtering methods) used can explain this difference. The measured skin roughness Ra at full forearm extension, however, was similar to roughness (7.2  $\pm$  1.3  $\mu\text{m}$ ) reported by Kottner et al. (2013).

Moreover, the mean roughness depth Rz of the DEJ decreased from 81.4  $\mu\text{m}$  to 40.4  $\mu\text{m}$  during the forearm angle change from flexion to extension (Table 4). Based on the definition (Eq. (8)), the mean roughness depth Rz represents the average maximum height of the DEJ roughness profile and concerns maximum height variations (peak-to-valley); therefore Rz probably overestimates a typical DEJ average thickness. For example, in a study by Neerken et al. (2004), the mean thickness of the DEJ of the forearm was found to be 25 and 41  $\mu\text{m}$  in older and younger skin, respectively, but was in both age groups lower than the Rz values measured in this case study in the 90° arm bending position. As mentioned before, due to the undulation of the dermal-epidermal junction, large differences can be obtained in epidermis layer thickness (Neerken et al., 2004) which in return will also affect the calculation of the DEJ thickness and undulation geometry parameters being defined by standard roughness parameters Ra and Rz in this article.

In this flexion-extension study, upon changing the forearm angle from 90° bending to 180° extension, the mean skin surface profile and DEJ geometry parameters (Ra, Rz) decreased to a similar extent by about 41–50% (Table 4). The observed similar percentage reduction in skin surface roughness and EDJ flatness/undulation (between 41–50%) upon natural skin stretching from 90° to 180° seems to be in agreement with the fact that these skin layers have the same in-plane strain because they are mechanically and structurally connected with each other. In this context, it should be pointed out that a systematic roughness offset may have been introduced into the measurement result due to the fact that in 90° bending position the skin was compressed and folded up, causing wrinkling, whereas the 180° full extension position may have led to pronounced skin stretching and epidermis flattening.

Skin is a hierarchical functionally graded multilayer composite in which different skin layers are firmly connected with each other and via tendons, fascia and muscles mechanically connected to bony structures (Gerhardt et al., 2012; Lamers et al., 2013). As skin is firmly connected to the underlying body tissue structures, when the multilayer composite is subjected to body movements and global stretch, it will consequently accommodate for the exposed strain and respond in such a way that both the epidermal-dermal junction flatten and skin surface asperities smoothen out.

According to Ferguson and Barbul (1981), during stretching of the skin the undulations of the epidermal surface and epidermal-dermal junction are flattened before elongation of the epidermal cells occurs. Moreover they suggested that the surface folds provide a reserve of tissue, allowing the epidermis to stretch without stretching or disrupting the epidermal cells. If this is true there should be a relationship between the skin extensibility and the grooves and ridges of the skin surface pattern which produce the functional epidermal reserve. Therefore, Ferguson and Barbul (1981) measured forearm skin roughness at varying strain and quantified how skin stretching reduces the roughness along the stretch direction. They found a gradual decrease in surface roughness Ra from 14 µm to 6 µm at 10–30% strain. This result is fully in line with our observations and data (Tables 3 and 4), showing a tendency to skin smoothing with increasing strain. Though, due to the limited strain and roughness data (only at 90° flexion and 180° extension) a mathematical correlation cannot be established in a sensible and reliable way.

As a final note, we would like to point out that although our epidermal and DEJ layer thickness detection algorithm has not been fully validated using for example histology, qualitative assessment of OCT images by several skin experts and authors of the present paper showed that the developed image code is sufficiently robust and sensitive to reliably identify and determine epidermis and DEJ thickness by automatic identification of skin structural features. Even if the code has not been fully validated, it allows reliable relative comparisons of skin layer thickness and geometry change during a flexion-extension experiment. However, as both the DEJ (basement membrane) and the papillary dermis are signal poor; whereas reticular dermis is signal intense (Welzel, 2014) it cannot be ruled out that some minor contributions of the papillary dermis are included in the epidermal thickness and DEJ flatness determination.

## 5. Study limitations and outlook

As the DIC and OCT measurement systems used were based at different locations, the experiments needed to be performed on different days and combined OCT and DIC measurement were not possible. However, care was taken that DIC and OCT images were taken at the same location with reference to a well-defined anatomical landmark (birth mark present at the volunteer's forearm). In addition, OCT based DIC sub-surface strain mapping (through plane skin layer strains distribution) (Sun et al., 2013) will need to be used to understand deformation and strain behaviour among different skin layers, and link skin surface strains to sub-surface strains and related geometry changes of the upper skin layers.

This OCT-DIC study was performed at two well-defined arm end positions, 90° flexion and 180° full extension. Further optimisation of the current OCT setup towards image registration is required to be able to perform dynamic measurements by gradually changing the arm angle and monitoring the evolution of epidermal thickness change and skin roughness/DEJ flatness as a function of skin surface strain measured by DIC.

The OCT system used in this study could not resolve the stratum corneum thickness sufficiently. In future, high speed

high resolution OCT systems will be used to acquire information on structural changes of the stratum corneum and better differentiate individual corneocyte cell layers of the stratum corneum and image the outermost skin layer after exposure to cyclic or static mechanical loading. To our knowledge, there is no standardised algorithm to determine epidermis and DEJ thickness from OCT images. Future research should also strive to come to a consensus on image algorithms to be used for more standardised and user-independent detailed clinical comparisons between OCT and physical biopsy or histology, especially related to visualisation and identification of the DEJ from OCT images.

This article describes a case study ( $n=1$ ) with a new image analysis algorithm to study feasibility to reliably quantify morphological skin parameters changes in skin from OCT images following natural stretching measured by DIC. Due to the large number of data points analysed (more than 700,000 data points for epidermis thickness and roughness data from OCT images, as well as about 3400 strain data from DIC measurements), it can be concluded that the feasibility to reliably quantify morphological parameters, surface strains and sub-layer deformation of volar forearm skin was demonstrated. However, the herein presented results are of limited nature and cannot be generalised for a specific population. They need to be confirmed by measurements on a larger sample size to be able to draw more general conclusions on the effect of natural skin stretching on morphological and topographical skin changes. Moreover, it would be very interesting to study the mathematical correlation between applied skin surface strain and surface roughness as well as epidermal-dermal junction flattening more quantitatively.

The newly developed method will be used to measure skin deformation behaviour of a larger study population to be able to draw more established general conclusions for gender, age, body location or skin disease. For example, our method is suggested to be a useful tool to study the effect of normal and shear load on the internal skin deformation behaviour to assess damage potential of external loading conditions with regard to blister or decubitus ulcer formation.

## 6. Conclusions

This case study demonstrated the feasibility to reliably quantify morphological skin parameters from OCT images. A new methodology was described, which combines two non-invasive techniques, namely DIC and OCT, to determine skin surface strain and sub-surface layer deformation of volar forearm. Changing the arm angle from natural flexion (90°) to full extension (180°) increased skin surface strains by typically 25%. These surface strains induced morphological changes in the upper skin layers, as evidenced by reduction of epidermal layer thickness (20%), decrease of the dermal-epidermal junction undulation roughness (45–50%) and skin surface roughness (40–50%). DIC combined with OCT imaging is a powerful and fast methodology to study real-time and non-invasively structural skin changes and the tissue response provoked by external mechanical loading.

## Acknowledgements

The research was supported in part by European Commission FP7 UNITIIS, FP7-PEOPLE-2011-1APP/286174 and Engineering and Physical Science Research Council, Research Council United Kingdom, EP/K009699/1. The authors would like to express their gratitude to Dr Peter Mäckel (isi-sys GmbH, Kassel, Germany) for technical support and valuable discussions on the DIC software and test setup.

## Appendix A. Supplementary material

Supplementary data associated with this article can be found in the online version at <http://dx.doi.org/10.1016/j.jmbbm.2016.05.035>.

## REFERENCES

- Abignano, G., Aydin, S.Z., Castillo-Gallego, C., Liakouli, V., Woods, D., Meekings, A., Wakefield, R.J., McGonagle, D.G., Emery, P., Del Gaidom, F., 2013. Virtual skin biopsy by optical coherence tomography: the first quantitative imaging biomarker for scleroderma. *Ann. Rheum. Dis.* 72 (11), 1845–1851.
- Affagard, J.S., Feissel, P., Bensamoun, S.F., 2015. Measurement of the quadriceps muscle displacement and strain fields with ultrasound and Digital Image Correlation (DIC) techniques. *IRBM* 36, 170–177.
- Alawi, S.A., Batzm, S., Räwert-Huber, J., Fluhr, J.W., Lademann, J., Ulrich, M., 2015. Correlation of optical coherence tomography and histology in microcystic adnexal carcinoma: a case report. *Skin Res. Technol.* 21 (1), 15–17.
- Aoi, N., Yoshimura, K., Kadono, T., Nakagami, G., Iizuka, S., Higashino, T., Araki, J., Koshima, I., Sanada, H., 2009. Ultrasound assessment of deep tissue injury in pressure ulcers: possible prediction of pressure ulcer progression. *Plast. Reconstr. Surg.* 124 (2), 540–550.
- Barbarino, G.G., Jabareen, M., Mazza, E., 2011. Experimental and numerical study on the mechanical behavior of the superficial layers of the face. *Skin Res. Technol.* 17 (4), 434–444.
- Barton, J.K., Gossage, K.W., Xu, W., Ranger-Moore, J.R., Saboda, K., Brooks, C.A., Duckett, L.D., Salasche, S.J., Warneke, J.A., Alberts, D.S., 2003. Investigating sun-damaged skin and actinic keratosis with optical coherence tomography: a pilot study. *Technol. Cancer Res. Treat.* 2 (6), 525–535.
- Bloemen, M.C., van Gerven, M.S., van der Wal, M.B., Verhaegen, P.D., Middelkoop, E., 2011. An objective device for measuring surface roughness of skin and scars. *J. Am. Acad. Dermatol.* 64 (4), 706–715.
- Buganza Tepole, A., Gart, M., Gosain, A.K., Kuhl, E., 2014. Characterization of living skin using multi-view stereo and isogeometric analysis. *Acta Biomater.* 10 (11), 4822–4831.
- Byers, R.A., Tozer, G., Brown, N.J., Matcher, S.J., 2016. High-resolution label-free vascular imaging using a commercial, clinically approved dermatological OCT scanner. In: Proceedings of the International Society for Optics and Photonics, SPIE San Francisco, 13–18 February.
- Coleman, A.J., Richardson, T.J., Orchard, G., Uddin, A., Choi, M.J., Lacy, K.E., 2013. Histological correlates of optical coherence tomography in non-melanoma skin cancer. *Skin. Res. Technol.* 19 (1), 10–19.
- Diridollou, S., Berson, M., Vabre, V., Black, D., Karlsson, B., Auriol, F., Gregoire, J.M., Yvon, C., Vaillant, L., Gall, Y., Patat, F., 1998. An in vivo method for measuring the mechanical properties of the skin using ultrasound. *Ultrasound Med. Biol.* 24 (2), 215–224.
- Egawa, M., Oquiri, M., Kuwahara, T., Takahashi, M., 2002. Effect of exposure of human skin to a dry environment. *Skin Res. Technol.* 8 (4), 212–218.
- Enfield, J., Jonathan, E., Leahy, M., 2011. In vivo imaging of the microcirculation of the volar forearm using correlation mapping optical coherence tomography (cmOCT). *Biomed. Opt. Express* 2 (5), 1184–1193.
- Evans, S.L., Holt, C.A., 2009. Measuring the mechanical properties of human skin in vivo using digital image correlation and finite element modelling. *J. Strain Anal. Eng. Des.* 44 (5), 337–345.
- Fercher, A.F., Drexler, W., Hitzenberger, C.K., Lasser, T., 2003. Optical coherence tomography- principles and applications. *Rep. Progress. Phys.* 66, 239–303.
- Ferguson, J., Barbenel, J.C., 1981. Skin surface patterns and the directional mechanical properties of the dermis (Chapter 10). In: Marks, R., Payne, P.A. (Eds.), *Bioengineering and the Skin*. Springer, pp. 83–92.
- Gambichler, T., Matip, R., Moussa, G., Altmeyer, P., Hoffmann, K., 2006. In vivo data of epidermal thickness evaluated by optical coherence tomography: effects of age, gender, skin type, and anatomic site. *J. Dermatol. Sci.* 44 (3), 145–152.
- Gambichler, T., Pljakic, A., Schmitz, L., 2015. Recent advances in clinical application of optical coherence tomography of human skin. *Clin. Cosmet. Investig. Dermatol.* 8, 345–354.
- Genovese, K., Montes, A., Martínez, A., Evans, S.L., 2015. Full-surface deformation measurement of anisotropic tissues under indentation. *Medical Engineering and Physics*. Vol. 37 (5), pp. 484–493.
- Gerhardt, L.-C., Schmidt, J., Sanz-Herrera, J.A., Baaijens, F.P.T., Ansari, T., Peter, G.V.M., Oomens, C.W.J., 2012. A novel method for visualising and quantifying through-plane skin layer deformations. *J. Mech. Behav. Biomed. Mater.* 14, 199–207.
- Greaves, N.S., Benatar, B., Whiteside, S., Alonso-Rasgado, T., Baguneid, M., Bayat, A., 2014. Optical coherence tomography: a reliable alternative to invasive histological assessment of acute wound healing in human skin? *Br. J. Dermatol.* 170 (4), 840–850.
- Hojjatoleslami, A., Avanaki, M.R.N., 2012. OCT skin image enhancement through attenuation compensation. *Appl. Opt.* 51 (21), 4927–4935.
- Hu, X., Maiti, R., Liu, X., Gerhardt, L.-C., Lee, Z.S., Byers, R., Franklin, S.E., Lewis, R., Matcher, S.J., Carré, M.J., 2016. Skin Surface and sub-surface strain and deformation imaging using optical coherence tomography and digital image correlation. In: Proceedings of the International Society for Optics and Photonics, SPIE San Francisco, 13–18 February.
- Huang, H.Y.S., Huang, S., Frazier, C.P., Prim, P., Harrysson, O., 2014. Directional biomechanical properties of porcine skin tissue. *J. Mech. Med. Biol.* 14 (5), 1450069.
- Jacobi, U., Chen, M., Frankowski, G., Sinkgraven, R., Hund, M., Rzany, B., Sterry, W., Lademann, J., 2004. In vivo determination of skin surface topography using an optical 3D device. *Skin. Res. Technol.* 10, 207–214.
- Jacquemoud, C., Bruyere-Garnier, K., Coret, M., 2007. Methodology to determine failure characteristics of planar soft tissues using a dynamic tensile test. *J. Biomech.* 40 (2), 468–475.
- Josse, G., George, J., Black, D., 2011. Automatic measurement of epidermal thickness from optical coherence tomography images using a new algorithm. *Skin Res. Technol.* 17 (3), 314–319.
- Kampf, G., Ennen, J., 2006. Regular use of a hand cream can attenuate skin dryness and roughness caused by frequent hand washing. *BMC Dermatol.* 6, 1.
- Kao, A.P., Connelly, J.T., Barber, A.H., 2016. 3D nanomechanical evaluations of dermal structures in skin. *J. Mech. Behav. Biomed. Mater.* 57, 14–23.

- Kottner, J., Schario, M., Garcia Bartels, N., Pantchevnikova, E., Hillmann, K., Blume-Peytavi, U., 2013. Comparison of two *in vivo* measurements for skin surface topography. *Skin Res. Technol.* 19 (2), 84–90.
- Kwiatsowska, M., Franklin, S.E., Hendriks, C.P., Kwiatkowski, K., 2009. Friction and deformation behaviour of human skin. *Wear* 267 (5–8), 1264–1273.
- Lademann, J., Otberg, N., Richter, H., Meyer, L., Audring, H., Teichmann, A., Thomas, S., Knutte, A., Sterry, W., 2007. Application of optical non-invasive methods in skin physiology: a comparison of laser scanning microscopy and optical coherent tomography with histological analysis. *Skin Res. Technol.* 13 (2), 119–132.
- Lamers, E., van Kempen, T.H.S., Baaijens, F.P.T., Peters, G.W.M., Oomens, C.W.J., 2013. Large amplitude oscillatory shear properties of human skin. *J. Mech. Behav. Biomed. Mater.* 28, 462–470.
- Li, L., Mac-Mary, S., Marsaut, D., Sainthillier, J.M., Nouveau, S., Gharbi, T., de Lacharriere, O., Humbert, P., 2006. Age-related changes in skin topography and microcirculation. *Arch. Dermatol. Res.* 297 (9), 412–416.
- Liu, X., Lu, Z., Lewis, R., Carré, M.J., Matcher, S.J., 2013. Feasibility of using optical coherence tomography to study the influence of skin structure on finger friction. *Tribol. Int.* 63, 34–44.
- Luther, N., Darvin, M.E., Sterry, W., Lademann, J., Patzelt, A., 2012. Ethnic differences in skin physiology, hair follicle morphology and follicular penetration. *Skin Pharmacol. Physiol.* 25 (4), 182–191.
- Mahmud, J., Holt, G.A., Evans, S.A., 2010. An innovative application of a small-scale motion analysis technique to quantify human skin deformation *in vivo*. *J. Biomech.* 43, 1002–1006.
- Neerken, S., Lucassen, G.W., Bisschop, M.A., Lenderink, E., Nuijs, T.A., 2004. Characterization of age-related effects in human skin: a comparative study that applies confocal laser scanning microscopy and optical coherence tomography. *J. Biomed. Opt.* 9 (2), 274–281.
- Ní Annaidh, A., Bruyère, K., Destrade, M., Gilchrist, M.D., Otténio, M., 2012. Characterization of the anisotropic mechanical properties of excised human skin. *J. Mech. Behav. Biomed. Mater.* 5 (1), 139–148.
- Obrupta, E.W., Newman, D.J., 2015. A comparison of human skin strain fields of the elbow joint for mechanical counter pressure space suit development. In: Proceedings of the Aerospace conference, IEEE 7–14, March.
- Ottieno, M., Tran, D., Ní Annaidh, A., Gilchrist, M.D., Bruyère, K., 2015. Strain rate and anisotropy effects on the tensile failure characteristics of human skin. *J. Mech. Behav. Biomed. Mater.* 41, 241–250.
- Paillet-Mattei, C., Bec, S., Zahouani, H., 2008. *In vivo* measurements of the elastic mechanical properties of human skin by indentation tests. *Med. Eng. Phys.* 30 (5), 599–606.
- Palanca, M., Tozzi, G., Cristofolini, L., 2016. The use of digital image correlation in the biomechanical area: a review. *Int. Biomech.* 3 (1), 1–21.
- Parsons, E., Boyce, M.C., Parks, D.M., 2004. An experimental investigation of the large-strain tensile behaviour of neat and rubber-toughened polycarbonate. *Polymer* 45 (8), 2665–2684.
- Pomerantz, R., Zell, D., McKenzie, G., Siegel, D.M., 2011. Optical coherence tomography used as a modality to delineate basal cell carcinoma prior to mohs micrographic surgery. *Case Rep. Dermatol.* 3 (3), 212–218.
- Proksch, E., Brandner, J.M., Jensen, J.M., 2008. The skin: an indispensable barrier. *Exp. Dermatol.* 17 (12), 1063–1072.
- Sattler, E.C., Kästle, R., Welzel, J., 2013. Optical coherence tomography in dermatology. *J. Biomed. Opt.* 18 (6), 061224.
- Sun, C., Standish, B., Vuong, B., Wen, X.-Y., Yang, V., 2013. Digital image correlation-based optical coherence elastography. *J. Biomed. Opt.* 18 (12), 121515 (9 pages).
- Sutton, M.A., 2008. Digital Image Correlation for Shape and deformation measurements (Chapter 20). In: William, N., Sharpe, Jr (Eds.), *Springer Handbook of Experimental Solid Mechanics*, pp. 565–600.
- Sutton, M.A., Orteu, J.J., Schreier, H., 2009. Digital Image Correlation (Chapter 5), In: Sutton M.A., Orteu J.J. and Schreier H., *Image Correlation for Shape, Motion and Deformation Measurements: Basic Concepts. Theory and Applications*, 81–116.
- Timoshenko, S., Woinowsky-Krieger, S., 1959. *Theory of Plates and Shells*. McGraw-Hill, New York.
- Trojahn, C., Dobos, G., Richter, C., Blume-Peytavi, U., Kottner, J., 2015. Measuring skin aging using optical coherence tomography *in vivo*: a validation study. *J. Biomed. Opt.* 20 (4) 045003-1–045003-6.
- Tsugita, T., Nishijima, T., Kitahara, T., Takema, Y., 2013. Positional differences and aging changes in Japanese woman epidermal thickness and corneous thickness determined by OCT (optical coherence tomography). *Skin. Res. Technol.* 19 (3), 242–250.
- Ulrich, M., von Braunmuehl, T., Kurzen, H., Dirschka, T., Kellner, C., Sattler, E., Berking, C., Welzel, J., Reinhold, U., 2015. The sensitivity and specificity of optical coherence tomography for the assisted diagnosis of nonpigmented basal cell carcinoma: an observational study. *Br. J. Dermatol.* 173 (2), 428–435.
- Weickenmeier, J., Wu, R., Lecomte-Grosbras, P., Witz, J-F., Brieu, M., Winklhofer, S., Andreisek, G., Mazza, E., 2014. Experimental Characterization and Simulation of Layer Interaction in Facial Soft Tissues. In: *Proceedings of the Biomedical Simulation 6th International Symposium, ISBMS*, Strasbourg, France, October 16–17.
- Weissman, J., Hancewicz, T., Kaplan, P., 2004. Optical coherence tomography of skin for measurement of epidermal thickness by shapelet-based image analysis. *Opt. Express* 12 (23), 5760–5769.
- Welzel, J., 2014. Optical coherence tomography. In: Berardesca, E., Maibach, H., Wilhelm, K.-P. (Eds.), *Non-Invasive Diagnostic Techniques in Clinical Dermatology*. Springer, pp. 35–40.
- VIC-3D v7 Testing Guide, accessed on 13th May 2016. <<http://www.correlatedsolutions.com/support/index.php?/Knowledgebase/Article/View/32/0/vic-3d-v7-testing-guide>>.
- Zafar, H., Enfield, J., O'Connell, M.L., Ramsay, B., Lynch, M., Leahy, M.J., 2014. Assessment of psoriatic plaque *in vivo* with correlation mapping optical coherence tomography. *Skin Res. Technol.* 20 (2), 141–146.
- Zahouani, H., Paillet-Mattei, C., Sohm, B., Vargiu, R., Cenizo, V., Debret, R., 2009. Characterization of the mechanical properties of a dermal equivalent compared with human skin *in vivo* by indentation and static friction tests. *Skin Res. Technol.* 15 (1), 68–76.
- Zhang, Y., Wu, G., Wei, H., Guo, Z., Yang, H., He, Y., Xie, S., 2014. Continuous non-invasive monitoring of changes in human skin optical properties during oral intake of different sugars with optical coherence tomography. *Biomed. Opt. Express* 5 (4), 990–999.